Experimental and theoretical study of single iron particle combustion under low-oxygen dilution conditions

Fuel 357 (2024) 129718

Contents lists available at ScienceDirect

Fuel

journal homepage: www.elsevier.com/locate/fuel

Full length article

Experimental and theoretical study of single iron particle combustion under low-oxygen dilution conditions

D. Ning *, T. Hazenberg, Y. Shoshin, J.A. van Oijen, G. Finotello, L.P.H. de Goey

Department of Mechanical Engineering, Eindhoven University of Technology, The Netherlands

ARTICLE INFO

Keywords:
Metal fuel
Iron particle combustion
Particle sizing
Theoretical burn time
Low-oxygen dilution

ABSTRACT

In the present study, a novel *in situ* particle sizing approach is proposed and used to measure the characteristic timescales of micron-sized iron particle combustion under low-oxygen (10–17 vol%) dilution conditions. The particle size is determined by probing the light emission intensity of a burning particle during melting, which is proportional to the cross-section area of the particle projected to the camera. Detailed descriptions of the calibration, validation, and characterization of the experimental method are elaborated. With systematic measurements, we obtain one-to-one correlations between combustion timescales and single particle diameters at various diluted oxygen concentrations. Furthermore, we formally derive a theoretical model for heterogeneous combustion of growing (iron) particles in the diffusion-limited regime. The model suggests that the diffusion-limited burn time scales with the initial particle diameter squared (i.e., a new, generalized d^2-law). Owing to accounting for the particle growth, the newly derived model suggests a significantly (1.66 times) shorter combustion duration compared to the conventional d^2-law for shrinking particle combustion. It turns out that the new model agrees well with the experiment. This agreement also suggests that under low-oxygen dilution conditions, the combustion regime of iron particles during the intensive burning stage (i.e., from ignition to the peak particle temperature) is limited by external oxygen diffusion.

1. Introduction

Driven by the imperative need for the energy transition and the intermittent nature of renewable energy sources, the demand for green energy storage and transportation have been increasing. Renewable energy carriers such as hydrogen, ammonia, and batteries has considerably lower energy densities compared to hydrocarbons, making them less efficient for producing heat and power in a compact way. Therefore, the pursuit for better alternatives encourages the introduction of innovative carbon-neutral energy conversion technologies. Recently, Bergthorson et al. [1] proposed the direct combustion of recyclable metal fuels for zero-carbon heat and power generation. The energy densities of most combustible metals are significantly higher than traditional fossil fuels. Historically, metal combustion already has successful applications, such as in rocket propellants, because of the high specific thrust [2]. Aside from military purposes, the energy released from metal combustion can also be used to power industries, domestic heating facilities, and heavy-duty transportation. The elimination of coal from the energy market provides an opportunity for metal fuels, as coal-fired power plants can be retrofitted to accommodate them [3]. The combustion products of metals, i.e., metal oxides, can be collected and reduced offsite using renewable energy. The closed loop of direct combustion-reduction of metal (oxides) powders forms a clean energy cycle (i.e., the so-called dry cycle [4]) with metal powder as the energy carrier that can easily be stored, transported, and traded.

Among all metal fuels, iron powder is considered a promising candidate for the dry cycle because of several advantages. (1) Micron-sized iron particles burn heterogeneously in air resulting in minor emission of nanoparticles, which enables the capture of the solid micron-sized iron oxide particles produced during combustion. (2) Unlike other metals such as Li, Mg, and Al that burn violently with potential safety risks, the combustion of iron is relatively gentle, resulting in a flame temperature comparable to that of hydrocarbons. (3) Sources of iron are multiple — it is the fourth most abundant element in Earth's crust. (4) Iron oxide can readily be recycled using hydrogen produced by renewable sources based on well-established technologies. For the successful application of iron as a recyclable carbon-free fuel, detailed experimental diagnostics of iron particle combustion must be conducted to gain deeper understanding of the underlying physics. Moreover, systematic experimental data are desired to support the numerical modeling of iron combustion. Both experimental and numerical research will play a significant role in the design of future iron-fueled combustors. However, unlike gaseous fuels and coal, of which the combustion theory and numerical

* Corresponding author.
E-mail address: d.ning@tue.nl (D. Ning).

https://doi.org/10.1016/j.fuel.2023.129718
Received 6 April 2023; Received in revised form 25 August 2023; Accepted 3 September 2023
Available online 18 September 2023

models have been well established, fundamental understanding on iron combustion is still very limited, which is one of main obstacles towards application of iron as a recyclable fuel.

Over the last two decades, experimental studies of iron particle combustion have been limited to the investigation of iron dust flames to gain statistical knowledge of observable quantities at a macroscale. Sun and his coworkers conducted a first series of experiments on iron/air flame propagation, temperatures, and individual particle behavior in iron aerosol flames [5–7]. However, their experiments only focused on particles with a relatively small diameter (around 1–8 μm). In practice, iron powders with a size distribution between 1–100 μm are usually encountered. Tang et al. [8] measured the flame speeds and quenching distances of freely propagating iron dust flames for iron powders with arithmetic mean particle diameters ($d_{1,0}$) within 3.3–26.8 μm. They observed that the flame speed is inversely proportional to the particle diameter, and the flame quenching distance increases linearly with increasing particle size. Based on the same setup, Tang et al. [9] studied the regimes of particle combustion in iron dust flames and argued that there is a transition from diffusion-limited combustion to the kinetic-limited for particles around 3 μm when N_2 in air is replaced by Ar or He. Tóth et al. [10] investigated the combustion behavior of pulverized sponge iron (PSI) particle groups burning in hot vitiated atmospheres. The results show that PSI mainly burns heterogeneously. Meanwhile, they claimed that a gas-phase micro-flame enveloping the particle was observed through shadowgraph images even when the particle temperature is still considerably lower than the boiling point of iron, which contradicts the Glassman's criterion of burning metals [11] and needs to be further examined. The first stabilized, flat iron dust flame was obtained using a counterflow configuration and fine iron powder (d_{90} = 2.5 μm) by McRae et al. [12]. By varying the composition of the oxidizer from $0.3O_2/0.7Ar$ to $0.4O_2/0.6Ar$ in the experiment, the flame speed was found to be independent on oxygen concentration, while the flame temperature increases from 2630 K to 2781 K. This, as claimed in the paper [12], implies that the flame propagation could be in the so-called discrete regime that occurs when the characteristic burn time of the particle is much shorter than the interparticle heat diffusion time [13–15]. However, a recent theoretical study by Ning and Shoshin [16] suggests that this insensitivity of flame propagation speed to the O_2 concentration (or the global reaction rate as particles burn faster at higher O_2 levels) is attributed to the large thermal inertia of the condensed phase. Therefore, single iron particle combustion plays a key role in the propagation of iron dust flames. Very recently, self-sustained Bunsen-type premixed and diffusion iron dust flames were established by Poletaev and Khlebnikova [17]. They observed that the fraction of iron-oxide nanoparticles in the combustion products increases with increasing oxygen concentration when particles burn in the diffusion regime at fuel lean conditions. This finding suggests that burning iron particles at low-oxygen dilution conditions could be a good strategy to minimize the nanoparticle formation.

To establish solid understanding of iron powder combustion, it is essential to gain insights into the burning characteristics of single iron particles. Therefore, dedicated experiments of isolated iron particle combustion have started to draw more attentions in recent years [18–26]. Some representative examples are discussed here. Wright et al. [27] were the first to measure single iron particles combustion in Ar/O_2 mixtures with a O_2 volume fraction between 21–60% at 1000 K. In this experiment, two timescales of the iron particle combustion process were evaluated: (1) the time to the maximum light emission intensity and (2) the total duration of incandescence. The results showed that both timescales strongly depend on the oxygen concentration and the experimental data deviate significantly from the classical d^2-law predictions. This suggests that the d^2-law, developed for shrinking droplet/particle combustion, might be invalid for iron particle combustion as the particle grows during burning [21]. Additionally, a spearpoint was observed near the end of combustion in their experiment. Similarly, Ning et al. [19] quantified the characteristic combustion duration of laser-ignited single iron particles at room temperature. They found that particles within 20–60 μm burn in the diffusion-limited regime until reaching the maximum brightness/temperature and hypothesized that there is still oxidation during particle cooling. This hypothesis has been further validated by observing that a particle has a considerably slower cooling rate after the peak temperature as compared to an inert particle [20]. Nevertheless, after the peak temperature, a further oxidation is very slow. This is suggested by the fact that particles maintain approximately a constant size instead of remarkably expanding before the peak temperature [21]. Additionally, it has been observed *in situ* that iron-oxide nanoparticle cloud formation of single burning particles is effectively suppressed by diluting the oxygen concentration [22], which agrees with the results of Poletaev and Khlebnikova [17] on an iron dust flame experiment. At TU Eindhoven, it has been suggested that moderate or intense low-oxygen dilution (MILD) combustion of metals could be the solution for optimal utilization of iron fuel for CO_2-free heating and power generation [28]. This method has the advantage of reducing both NOx and nanoparticle emissions, contributing to a near-zero-emission combustion process. This innovative metal combustion concept has been successfully demonstrated in a laboratory scale, 5 kW, MILD Cyclonic Combustor (MC^2) fueled with recycled iron powders [29]. Unfortunately, no systematic experimental investigation focusing on single iron particle combustion under low-oxygen dilution conditions has been reported yet to the best of our knowledge. This hurdles not only our further understanding of iron combustion under MILD conditions but also the development of iron-particle-combustion models for multi-dimensional computational fluid dynamics (CFD) simulations of laboratory and industrial scale iron-fueled MILD combustors.

The purpose of this work is, on the one hand, to perform detailed measurements to extend the knowledge of single iron particle combustion at low-oxygen dilution conditions. The established systematical, experimental database of iron particle burn time, a key parameter of single iron particle combustion, is of particular importance and valuable for the validation of iron particle reaction-transport models. On the other hand, we aim to develop a theoretical model to improve our understanding of the burn times of iron particles. This is inspired by the fact that the classical d^2-law has shown its significant over-prediction on the combustion duration of iron particles [27] but a justified model has not been formally derived. The paper is organized as follows. The characterization of the iron powders used in this study, experimental setup, and the particle sizing approach are introduced in Section 2. In Section 3, the proposed experimental method of particle-size-resolved burn time measurement is validated and the features of this method are discussed. In Section 4, the light emission profile, characteristic combustion duration as a function of particle diameter are reported. In Section 5, the derivation of a theoretical model for the burn times of growing (iron) particles in the diffusion-limited, heterogeneous combustion regime is presented. Moreover, the model is compared with the current experiment, by which the combustion regime of micron-sized iron particles under low-oxygen dilution conditions is identified. Finally, the main conclusions are summarized in Section 6.

2. Materials and experimental methodology

2.1. Materials

In the current experiment, two types of iron powders with purity larger than 99% are used to investigate the characteristic combustion timescales of single iron particles at diluted oxygen concentrations. As shown in Fig. 1, particles in these two powders present different morphology. The particles shown in Fig. 1(a), provided by TLS Technik GmbH & Co. (nominal diameter of 20–50 μm), have a nearly spherical shape and no observable porosity. In contrast, the sponge iron particles shown in Fig. 1(b), provided by CNPC Powder Group Co., Ltd. (powder

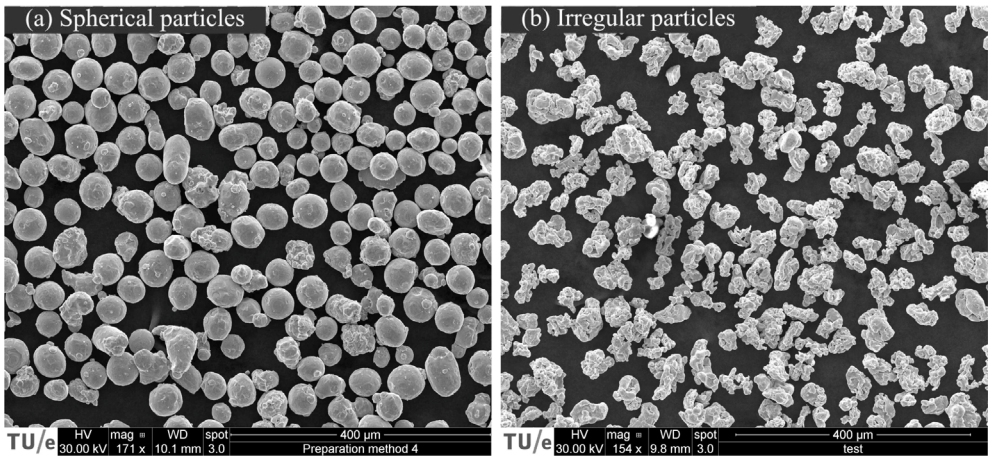

Fig. 1. SEM images of adopted iron powders with nearly spherical (a) and irregular (b) particle shapes.

type: CNPC-300, average equivalent diameter of 45 µm), have very irregular shapes and obvious porosity. Based on the morphology, the particles from these two commercial powders will be referred to as spherical and irregular particles in the following sections, respectively. The spherical particles will be used for most parts of the present work, while the irregular particles are used intentionally only for demonstrating the usability of the proposed particle sizing approach in measuring the combustion time of irregular particles as a function of volume-equivalent diameters.

2.2. Experimental setup and operation

As illustrated schematically in Fig. 2(a), the experimental setup adopted in the current study includes a single particle generator, a laser ignition system, and a high-speed COMOS camera (Photron SA3). Since the detailed description of the setup has been elaborated in our previous work [19,20], it will be only introduced concisely here. Micron-sized iron particles are ejected individually by an electrostatic particle generator (ESPG). The ESPG consists of a dispersion chamber where iron powder is aerosolized by a high voltage (around 3 kV) DC electrical field between two parallel electrodes. Dispersed iron particles are carried out the chamber by a stream of gas flow (central jet) through a bronze capillary tube (ID = 0.45 mm) located at the center of the top electrode. A 915 nm CW diode laser with an output power of 24 W is focused at approximately 1 mm above the tip of the capillary tube to ignite ejected single iron particles. The laser power is optimized by slowly increasing the energy of the laser beam until iron particles are reliably ignited. This procedure avoids the interference with the particle combustion process through excessive radiation energy. Moreover, it has been found in our previous work [19] that the residence times of the same type of iron particles in the laser beam are much shorter than the self-sustained combustion time. Thus, using the carefully selected laser power, the effect of laser heating on the measured particle burn time is minor. The burning particles are isolated from ambient air by a 20 mm-in-diameter co-axial shroud flow with composition identical to the central jet. Besides, the shroud flow maintains the velocity of ignited particles, making them move vertically upwards. The velocities and compositions of the central jet and shroud flow are regulated using mass flow controllers. During operation, the velocities of the central jet and shroud flow are set to 70 cm/s and 50 cm/s, respectively. The compositions of both flows are simultaneously adjusted in a range of 8–21 vol% oxygen diluted by nitrogen. Moreover, the uncertainty in O_2 volumetric fractions is around ±0.5%, examined using a calibrated gas analyzer.

Incandescent iron particles burning at different oxygen concentrations are imaged by the monochromatic high-speed camera equipped with an Irix 150 mm macro lens. A 850 nm interference band-pass filter with a full width at half maximum (FWHM) of 10 nm is employed to effectively filter out the particle-scattered laser light from the high speed camera. The high speed camera operates at a frame rate of 2 KHz, which is sufficient to resolve the transient process of iron particle combustion. Due to the large aperture ($f/2.8$) and relatively long exposure time (0.5 ms), the use of the narrow band-pass filter has no noticeable influence on the measurement of particle burn time, as compared to a 875 nm short-pass filter adopted in our previous study [19]. Fig. 2(b) shows a typical example of a temporally superimposed burning particle trajectory, where every bright spot represents the incandescent particle at a different moment.

2.3. Data processing and particle sizing

Before saturation of image pixels, the integrated pixel intensity, I_p, over the bright spot of an incandescent particle in an image can be expressed as

$$I_p = \alpha A_p \int_{\Delta\lambda} \varepsilon_\lambda(T_p) I_{\lambda,b}(T_p) d\lambda, \tag{1}$$

where α is the instrument constant, which is a combination of the effective transmissivity of all optical components, the spectrum sensitivity of the camera, spatial parameters such as the distance between the object and the camera and angle of view; A_p is the particle projection area in the camera direction, ε_λ and T_p are the spectral emissivity and temperature of the particle surface, respectively, and $I_{\lambda,b}$ is the spectral intensity of black body radiation. Assuming that T_p and ε_λ remain constant during particle melting, $\int_{\Delta\lambda} \varepsilon_\lambda(T_p) I_{\lambda,b}(T_p) d\lambda \approx \varepsilon_\lambda(T_p) I_{\lambda,b}(T_p) \Delta\lambda$ is constant when the bandwidth, $\Delta\lambda$, of the adopted interference filter is narrow. Therefore, a proportional correlation between initial particle diameter, d_0, and the light emission intensity during particle melting, I_{mp}, can be expressed as

$$d_0 = \beta \sqrt{I_{mp}}, \tag{2}$$

where β is the calibration coefficient that needs to be determined experimentally.

To calibrate the coefficient β, an independent experiment is conducted. The cold spherical iron particles ejected from the single particle generator are collected, and then the size distribution is measured by taking images with a calibrated optical microscope and processing them using the ImageJ software [30]. In this way, the error in calibration caused by the potential selective effect of ESPG on single particle generation can be avoided. This procedure is repeated a few times, and a consistent particle size distribution is obtained. Fig. 3 shows a histogram illustrating the size distribution of the spherical iron particles.

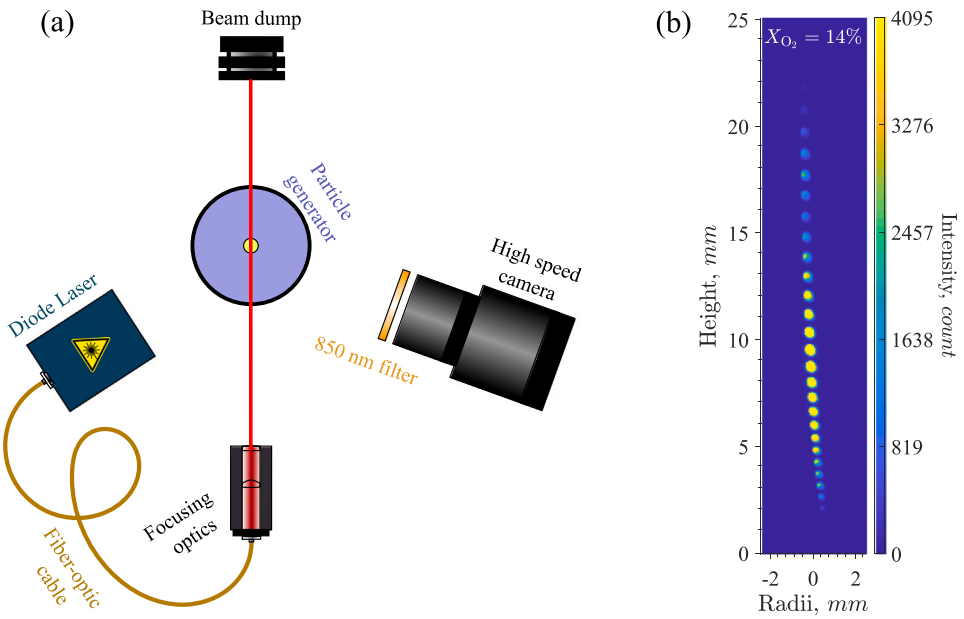

Fig. 2. (a) Schematic of the experimental setup. (b) Typical composite trace of particle combustion (color scale is added artificially to indicate the light emission intensity of the burning particle.). (For interpretation of the references to color in this figure legend, the reader is referred to the web version of this article.)

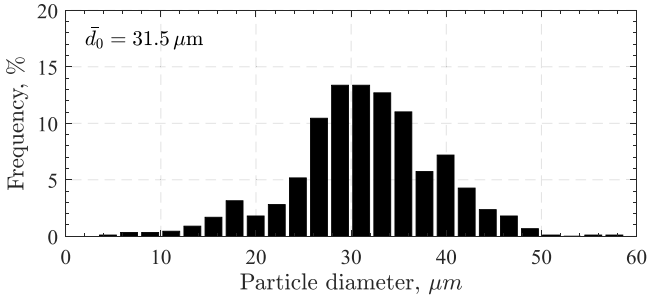

Fig. 3. Particle size distribution of cold TSL powder ejected from the particle generator. The measured average particle diameter ($\bar{d}_0$) is 31.5 μm.

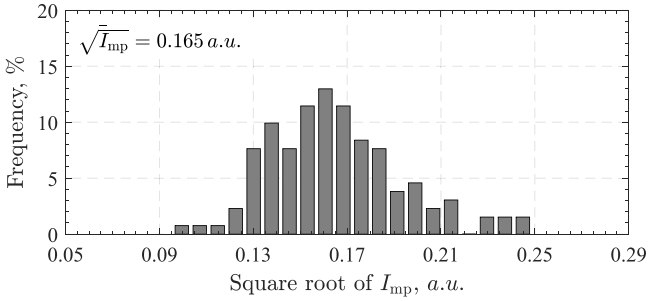

Fig. 4. Distribution of the square root of light emission intensity during particle melting. The measured mean value of the square root of I_{mp}, $\overline{\sqrt{I_{mp}}}$, is 0.165 in an arbitrary unit.

Approximately 95% of the particles are in the range of 15–45 μm, and the arithmetic mean particle diameter is 31.5 μm.

Afterwards, histories of light emission from burning particles are recorded using the high speed camera. Then the light emission intensity during particle melting (cf. the small plateau on the intensity profile shown in Fig. 8), I_{mp}, is probed automatically by looking for the local nearest-zero point of the first order derivative. The small number of particles, whose melting processes are not detected are discarded. The square root of each I_{mp} is calculated and the distribution of their values in an arbitrary unit is illustrated by the histogram in Fig. 4. To determine β, the arithmetic mean value of $\overline{\sqrt{I_{mp}}}$ is calculated based on the distribution. Finally, the ratio between the mean particle diameter and the average value of $\overline{\sqrt{I_{mp}}}$ distribution gives the required calibration coefficient β.

3. Validation, characterization, and uncertainty of particle sizing

In this section, the proposed particle sizing approach will be validated. Besides, the capability of the approach for sizing irregular particles will be presented. Finally, we will analyze the measurement uncertainty of the current particle sizing method.

3.1. Validation

After calibrating the coefficient β, the measured I_{mp} can be readily converted to the particle diameter using Eq. (2). The data in Fig. 4 are converted into the particle size distribution (PSD) to be directly comparable to the data shown in Fig. 3. Fig. 5 shows the comparison between the cumulative PSDs that are translated from Figs. 3 and 4. The two PSDs match quite well, although a slightly larger disagreement is observed when particles are smaller than approximately 25 μm. This is mainly because the melting process of the relatively small particles (~< 20 μm) are too short to be resolved by the current temporal resolution of the high speed camera. Nevertheless, due to the fairly low population of particles smaller than 20 μm, the error introduced into the calibration coefficient β by the unresolved particles is insignificant, which can also be validated as will be described next.

To further validate the currently proposed experimental method, the duration of intensive combustion (i.e., t_{max}, defined as the time between the initially lowest detectable brightness to the peak light emission intensity, I_{max}) of burning iron particles, measured using the present method, are compared with data reported previously in [19], where sieved narrow size fractions were adopted. As reported in our previous work [19], the ignited particles can be detected by the camera at a location very close to or within the laser beam. When the burning particle is initially detected, the time elapsed since ignition is approximately shorter than 1 ms estimated based the residence time of a 50 μm in the laser beam. Therefore, t_{max} can accurately represent the combustion duration since ignition until the peak temperature. As shown in Fig. 6, a correlation between t_{max} and the particle diameters is

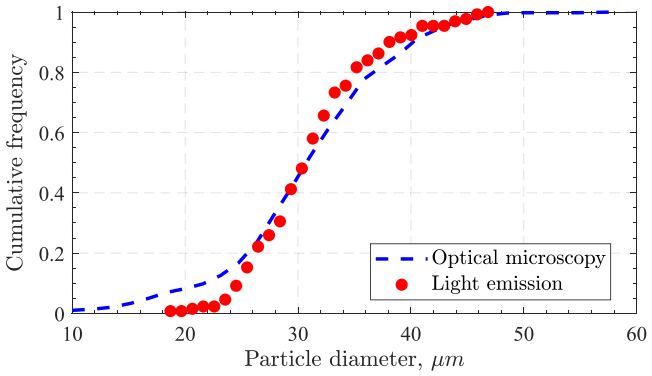

Fig. 5. Comparison between cumulative particle size distributions measured by using optical microscopy and light emission intensity during melting.

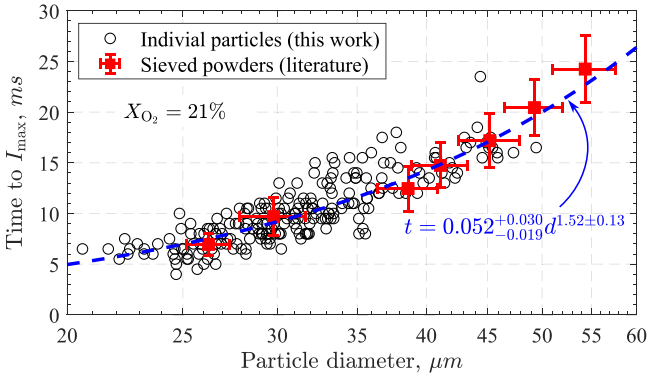

Fig. 6. Comparison of time to I_{max} as a function of particle diameter obtained using *in situ* sizing of individual particles and sieved powders reported in [19]. The blue dashed curve is the fitted trendline for all individual particles, which follows the mathematical expression in blue. The plus and minus tolerances in the mathematical expression correspond to the upper and lower bounds of 95% confidence for the fitting, respectively.

determined by fitting all data points, representing individual particles, into a power law. The fitted trendline shows good agreement with the previous measurement using sieved narrow size fractions.

3.2. Characterization

Besides easy-to-implement, another feature of the proposed measurement approach is that the particle diameter is determined for a truly spherical particle even though the original particle shape is highly irregular. This is because the irregularity of the initial particle shape is quickly diminished by surface tension once melting starts [25]. Therefore, the error introduced by nonsphericity in some other methods of particle-diameter measurements, such as [31,32], can be eliminated and the measured diameter is actually volume-equivalent. As a result, the current sizing approach is usable for nonspherical particles as well. To demonstrate this, t_{max} of the irregular particle batch, shown in Fig. 1(b), burning at 21 vol% O_2, is measured and compared with that of the spherical particles burning under the same condition (i.e., the trendline shown in Fig. 6). Fig. 7 shows that the measured t_{max} of irregular iron particles matches that of spherical particles fairly well although a small discrepancy is observed. Therefore, the current approach has shown to be effective in determining the correlation between the characteristic combustion time and diameter for irregular iron particles. Furthermore, this approach is well suited for burn time measurements of hydrogen-reduced iron particles, which have different porosity determined by differences in reduction temperature [33].

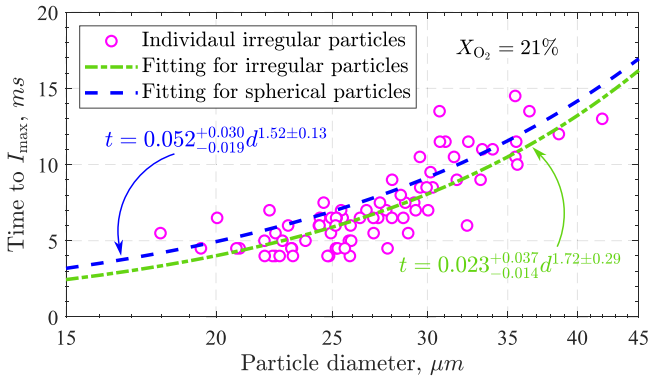

Fig. 7. Time to I_{max} of the irregular iron particles as compared to that (trendline) of the spherical particles. Each hollow dot represents an irregular particle. The blue dashed curve is the fitted trendline of t_{max} for spherical particles, and the green dash-dotted curve is the fitted trendline of t_{max} for irregular particles. The mathematical expressions of the fittings are embedded in the figure. The plus and minus tolerances in the mathematical expressions correspond the upper and lower bounds of 95% confidence for the fittings, respectively. (For interpretation of the references to color in this figure legend, the reader is referred to the web version of this article.)

3.3. Uncertainty

Despite the good quality of the proposed particle sizing approach, the measurement of particle sizes has uncertainties. The main sources of uncertainty are two-folds including the uncertainty of the calibration coefficient, β, and that of the I_{mp} measurement. The measurement uncertainty of $\bar{d}_0$, estimated by the standard deviation of three independent measurements, is ±5%. Similarly, the uncertainty of $\sqrt{\bar{I}_{mp}}$, is about ±7%. Therefore, the uncertainty of β is ±9% evaluated based on the error propagation function. The second major uncertainty of the individual particle size measurement is attributed to the error in the measurement of I_{mp}. Owing to the noise and finite spatial resolution of the imaging system, the measured light emission intensity at different positions on the melting plateau varies by approximately ±9%. According to the error propagation for Eq. (2), the overall uncertainty of the particle size measurement is around ±10%.

4. Experimental results

The proposed experimental method is applied to the measurement of the characteristic timescales of iron particles combusting under low-oxygen dilution conditions. The obtained experimental results will be presented and discussed in this section.

4.1. Light emission profiles

The light emission profiles reveal key information on the reaction rate and phase transitions occurring during iron particle combustion. Representative light emission profiles of iron particles burning at several diluted oxygen concentrations are shown in Fig. 8. The profiles are selected based on similar particle diameters, determined using Eq. (2), to directly observe the effect of oxygen concentration on the iron burning process with minimal influence of the particle size.

Except for the case of 8 vol% O_2, the profiles always feature double peaks and have a short plateau in the early stage of combustion due to particle melting [20,34]. The height of the first peak decreases with reducing oxygen concentrations, meaning that the maximum particle temperature decreases. On the contrary, the height of the second peak is not affected by the oxygen level as the particle temperature at this point is determined by the phase transition of oxygen-over-saturated, liquid iron oxide [20]. Furthermore, both the melting plateau and t_{max} become longer with decreasing oxygen concentration, suggesting that iron particles burn mildly under a diluted oxygen condition. However,

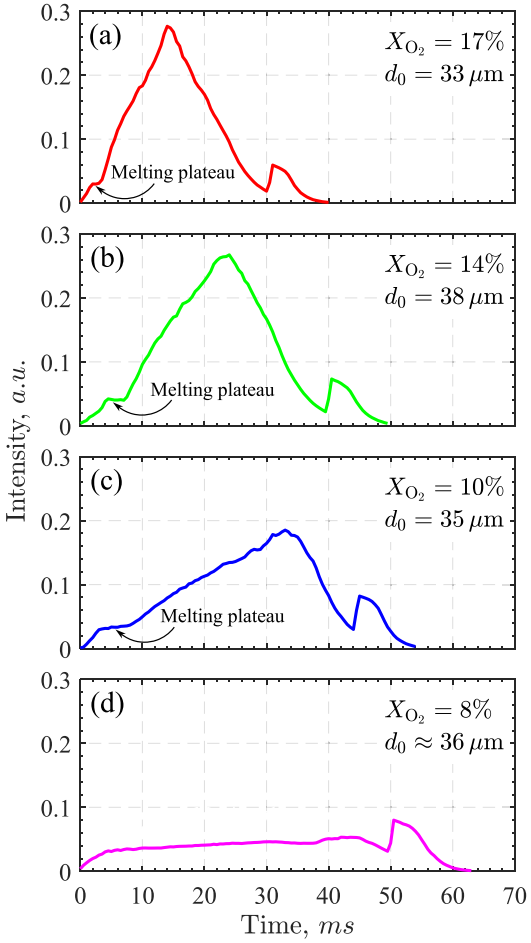

Fig. 8. Representative light emission profiles of burning iron particles in O_2/N_2 mixtures with volumetric oxygen concentrations of (a) 17 vol%, (b) 14 vol%, (c) 10 vol%, and (d) 8 vol%, respectively. The small plateau at the beginning of particle combustion corresponds to the melting process [20].

the time from I_{max} to the end of light emission (i.e., reactive cooling time) shows an opposite trend because the particle needs less time to cool down from a lower peak temperature.

For the case of 8 vol% O_2, instead of a clear transition between particle melting and later liquid-phase combustion, observed at relatively high oxygen concentrations, a long plateau-like stage with a very weak intensity increase is found. Additionally, it is common to observe that the second peak exceeds the previous plateau. This phenomenon suggests that the melting of the iron core stabilizes particle temperature almost till the end of combustion and the intensity increase is mainly attributed to the gradual particle expansion [21]. The particle temperature just slightly increases when iron core melts completely. After iron is fully consumed, the further oxidizing reaction, $FeO(l) + O_2(g) = Fe_3O_4(l)$, slows down and temperature decreases until a degree below the melting point of Fe_3O_4 (i.e., overcooling). Upon the rapid solidification, the particle temperature increases to the melting point of Fe_3O_4 due to the latent heat release. This scenario agrees with the fact that the first peak of intensity decreases and shifts toward the end of combustion as the O_2 content in the surrounding gas decreases. Due to the lack of a clear melting plateau, it is difficult to automatically size particles burning under this condition. Therefore, characteristic combustion times as a function of particle diameter are not quantified at 8 vol% O_2. Besides, the particle size in Fig. 8(d) for 8 vol% O_2 is estimated using the light emission intensity at 10 ms, when the particle is expected to undergo melting.

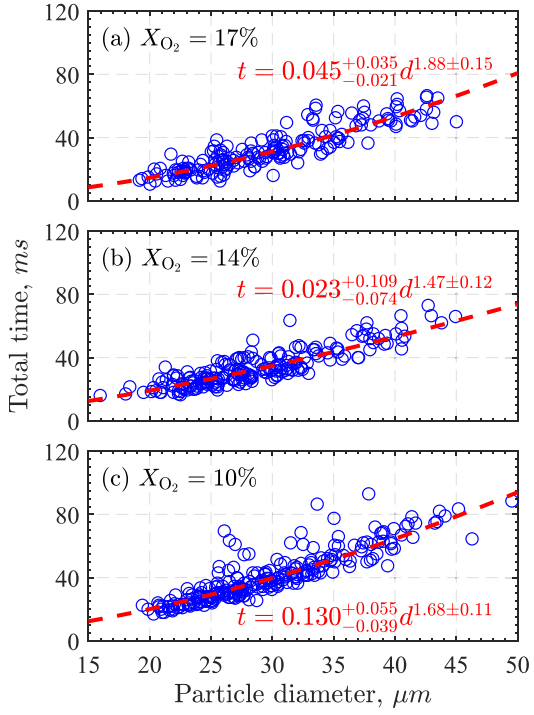

Fig. 9. Total time of light emission (t_{tot}) from burning iron particles as a function of the particle diameter at (a) 17 vol%, (b) 14 vol%, and (c) 10 vol% O_2, respectively. The plus and minus tolerances in the mathematical expressions correspond to the upper and lower bounds of 95% confidence for the fittings, respectively.

4.2. Characteristic timescales

Two characteristic times scales of iron particle combustion are extracted from the thermal emission profiles, namely time to I_{max} (t_{max}) and the total duration of light emission (t_{tot}) of the burning particles. The timescales t_{tot} represents the overall heat release time including an intensive combustion stage where fast heat release increases the particle temperature, as well as a reactive cooling stage characterized by weak heat release smaller than the heat loss mainly due to conduction. The timescale t_{max} characterizes the intensive combustion stage where most chemical energy is released by iron oxidization. The measured characteristic timescales are summarized in Figs. 9 and 10, showing a clear trend of increasing values with increasing particle diameter.

The correlations between the characteristic timescales and particle diameter are determined by fitting the experimental data of all single-particle-combustion events into the power law. The correlations predict the most confident characteristic times as a function of the initial particle diameter. Besides the experimental data, trendlines representing the power-law correlations for each O_2 concentration are also shown as dashed lines in Figs. 9 and 10. As depicted in Fig. 9, t_{tot} increases with increasing particle diameter, which follows a d^n tendency with $n \in [1.47 \pm 0.12, 1.87 \pm 0.15]$. Very similarly, Fig. 10 shows that t_{max} becomes longer for larger particles with a correlation described by d^n with $n \in [1.48 \pm 0.11, 1.72 \pm 0.23]$. The fitted exponents are similar to those found at normal and elevated oxygen concentrations [19].

5. Theoretical analysis and discussion

As revealed by the previous experiments [19], at normal and elevated oxygen concentrations, t_{max} is nearly proportional to the inverse of the oxygen concentration, which implies that the intensive combustion stage of iron particle at room temperature is limited by external oxygen diffusion. This experimental evidence enables numerical modeling of the combustion of a single particle without the need for

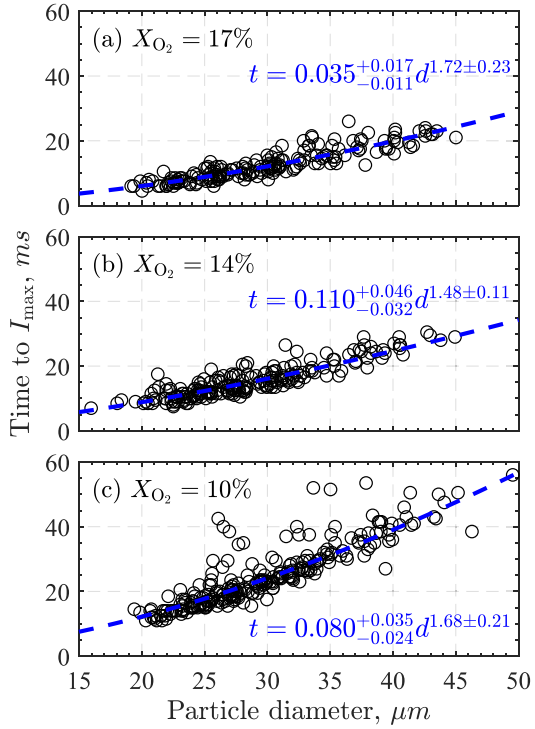

Fig. 10. Time to I_{max} of burning iron particles as a function of particle diameter at (a) 17 vol%, (b) 14 vol%, and (c) 10 vol% O_2, respectively. The plus and minus tolerances in the mathematical expressions correspond to the upper and lower bounds of 95% confidence for the fittings, respectively.

detailed information on the surface chemical reaction kinetics. When the oxygen concentration in the surrounding gas phase decreases, the particle surface temperature decreases if the particle combusts in a mainly diffusion-dominated regime, although it might not necessarily be limited by external O_2 diffusion. The rate of external oxygen diffusion to the iron particle surface is approximately proportional to $T_f^{0.7}$, in which T_f is the temperature at a virtual film layer. T_f is a reference temperature needed to calculate the oxygen mass diffusion to the particle surface [35]. When the particle temperature decreases, the kinetic rate of the surface chemical reaction could decrease much faster (exponentially) than the external oxygen diffusion rate if we assume a first order Arrhenius-type surface reaction suggested by Frank–Kamenetskii [36]. It is possible that the particle combustion regime shifts to an intermediate regime when the external oxygen concentration is below a certain value. It is worth to mention that at the room temperature, particles cannot burn in the kinetic-limited regime where the diffusive heat loss is much larger than the chemical heat release. Therefore, it is necessary to identify the combustion regime of single iron particles burning at diluted oxygen concentrations since the heterogeneous surface oxidation kinetics of liquid iron is still unclear. To this end, we will develop a basic theoretical model describing the diffusion-limited burn time of non-volatile[1] (iron) particles. Next, the experimental data will be compared with the model, which not only clarifies whether or not the combustion regime of iron particles under low O_2 dilution conditions is diffusion-limited but also validates the theoretical model.

5.1. Analytical model of diffusion-limited burn time

Under low O_2 dilution conditions, both the iron particle and its combustion product, iron oxide, are non-volatile. As a result, the particle mass increases by consuming oxygen, which is mathematically described as

$$\frac{\mathrm{d}}{\mathrm{d}t}\left(\frac{\pi}{6}\rho_\mathrm{p} d_\mathrm{p}^3\right) = \dot{m}_{O_2}, \tag{3}$$

where ρ_p and d_p are the density and diameter of the particle, respectively, and $\dot{m}_{O_2}$ is the consumption rate of O_2. As derived in Appendix, ρ_p is a function of particle diameter:

$$\rho_\mathrm{p} = \rho_1 + \left(\frac{d_0}{d_\mathrm{p}}\right)^3 \rho_2 \tag{4a}$$

with

$$\rho_1 = \frac{\rho_\mathrm{b}}{1 + \mathcal{S}(1-\tau)} \tag{4b}$$

and

$$\rho_2 = \frac{\left(1+\mathcal{S}^{-1}\right)\left(\rho_\mathrm{u} - \rho_\mathrm{b}\right)}{1 + \mathcal{S}(1-\tau)}, \tag{4c}$$

where ρ_u and ρ_b are the density of unburned (iron) and burned (iron oxide) particle compositions at the room temperature (i.e., thermal expansion is neglected), $\mathcal{S}$ is the stoichiometric ratio in kg iron per kg oxygen, $\tau = \rho_b/\rho_u$ is the ratio of densities, and d_0 is the initial particle size. In the diffusion-limited combustion regime, the mass fraction of O_2 at the particle surface vanishes and hence $\dot{m}_{O_2}$ is calculated as

$$\dot{m}_{O_2} = \mathrm{Sh}\pi d_\mathrm{p}\left(\rho_g \mathcal{D}_{O_2,\mathrm{m}}\right)_\mathrm{f} Y_{O_2,\infty}, \tag{5}$$

where Sh is the Sherwood number, $\left(\rho_g \mathcal{D}_{O_2,\mathrm{m}}\right)_\mathrm{f}$ is the mass diffusivity of O_2 evaluated at the particle film layer, and $Y_{O_2,\infty}$ is the mass fraction of O_2 in the bulk. Substituting Eqs. (4) and (5) back to Eq. (3) and assuming Sh = 2 gives

$$\frac{\mathrm{d}d_\mathrm{p}^3}{\mathrm{d}t} = 12 d_\mathrm{p}\frac{\left(\rho_g \mathcal{D}_{O_2,\mathrm{m}}\right)_\mathrm{f}}{\rho_1} Y_{O_2,\infty}. \tag{6}$$

Note that the term with ρ_2 in ρ_p drops out as d_p^3 cancels d_p^{-3}. Solving Eq. (6) and applying the initial conditions, the particle's diameter can be related to time:

$$d_p^2 = d_0^2 + Kt \tag{7a}$$

with constant

$$K = 8\frac{\left(\rho_g \mathcal{D}_{O_2,\mathrm{m}}\right)_\mathrm{f}}{\rho_1} Y_{O_2,\infty}. \tag{7b}$$

The stoichiometric ratio and the initial mass of iron are known, thus the final particle diameter is given by

$$d_\mathrm{end}^2 = \left[\tau^{-1} + (\mathcal{S}\tau)^{-1}\right]^{2/3} d_0^2. \tag{8}$$

This result can be substituted into Eq. (7a) and the burn time, t_b, can be isolated, giving

$$t_b = \frac{d_\mathrm{end}^2 - d_0^2}{K} = \frac{d_0^2}{K_\mathrm{eff}} \tag{9a}$$

with constant

$$K_\mathrm{eff} = 8\frac{\left(\rho_g \mathcal{D}_{O_2,\mathrm{m}}\right)_\mathrm{f}}{\rho_\mathrm{u}} Y_{O_2,\infty}\mathcal{S}\cdot\frac{\tau^{-1} + (\mathcal{S}\tau)^{-1} - 1}{\left[\tau^{-1} + (\mathcal{S}\tau)^{-1}\right]^{2/3} - 1}. \tag{9b}$$

Eq. (9a) indicates that the particle burn time scales with the square of the initial particle diameter in the diffusion-limited regime (i.e., d^2-dependence). The exact d^2-dependence has not been found experimentally, which is likely due to measurement uncertainties in experiments and other secondary effects. Furthermore, Eq. (9a) is a generalized d^2-law for heterogeneous particle combustion. This generalization may account for both changes in density and the chemical incorporation of oxygen into the particle. The first part of Eq. (9b) is identical to the conventional d^2-law for shrinking char particle combustion. This

[1] Here by non-volatile, we strictly mean that both the fuel and reaction products are non-volatile.

part accounts for the rate of fuel consumption by O_2 diffusing onto the particle surface. The second part includes the effect due to the changing particle diameter, which is exclusively dependent on the reactant and product. Careful analysis reveals that it is the ratio of relative volume change to surface change. At two limiting conditions, the burn time of particles with constant and shrinking diameter can be derived from Eq. (9a), respectively. When $d_{end} = d_0$ (i.e., $\tau = 1 + S^{-1}$), the equation for K_{eff} of a constant-diameter particle is obtained by taking the limit of Eq. (9b) with L'Hôpital's rule:

$$\lim_{\tau \to 1+S^{-1}} K_{eff}(\tau) = 12 \frac{\left(\rho_g \mathcal{D}_{O_2,m}\right)_f}{\rho_u} Y_{O_2,\infty} S. \tag{10}$$

When $d_{end} = 0$ (i.e., $\tau \to \infty$), the second part of Eq. (9b) is unity and hence, K_{eff} of the classical d^2-law is recovered:

$$\lim_{\tau \to \infty} K_{eff}(\tau) = 8 \frac{\left(\rho_g \mathcal{D}_{O_2,m}\right)_f}{\rho_u} Y_{O_2,\infty} S. \tag{11}$$

For iron, assuming that FeO is formed until the particle peak temperature [37,38], the parameters are given by $S = 3.49$ and $\tau = 0.73$. As such, compared to the classical d^2-law applied to iron particles (see [27]), this generalized model suggests a 1.66 (the ratio between Eqs. (9b) and (11)) times shorter combustion duration due to particle growth.

5.2. Comparison between the theory and experiments

It has been explicitly indicated by Eqs. (9a) and (9b) that in the diffusion-limited combustion regime,

$$t_b \propto \frac{1}{\left(\rho_g \mathcal{D}_{O_2,m}\right)_f Y_{O_2,\infty}} \tag{12}$$

because the other parameters in Eqs. (9a) and (9b) are constant. The denominator in Eq. (12) is the mass-diffusion flux of O_2 to the particle surface. To identify the combustion regime of iron particles during the intensive combustion stage at low oxygen concentrations, the currently measured t_{max} and those acquired in the previous experiment [19] at normal and elevated oxygen concentrations are plotted together as a function of the inverse O_2 mass-diffusion flux in Fig. 11(a). The mass-diffusion flux is calculated using the corresponding O_2 mass fraction and the O_2 mass diffusivity at the film layer, i.e., $\left(\rho_g \mathcal{D}_{O_2,m}\right)_f$. As shown by a recent study, the 1/2 rule performs better than the 1/3 rule for iron particle combustion [39]. Thus, we estimate $\left(\rho_g \mathcal{D}_{O_2,m}\right)_f$ at a reference gas composition and a constant temperature given by the 1/2 rule, respectively:

$$Y_{O_2,f} = Y_{O_2,p} + \left(Y_{O_2,\infty} - Y_{O_2,p}\right)\Big/ 2, \tag{13}$$

and

$$T_f = \langle T_p \rangle + \left(T_g - \langle T_p \rangle\right)\Big/ 2 \tag{14}$$

with

$$\langle T_p \rangle = \left(T_{p,mp} + T_{p,max}\right)\Big/ 2, \tag{15a}$$

where $Y_{O_2,p}$ and $Y_{O_2,\infty}$ are the mass fractions of oxygen at the particle surface and in the bulk, respectively. $\langle T_p \rangle$ is the time-averaged particle temperature, approximated by averaging the melting point ($T_{p,mp}$ = 1809 K) and the peak temperature ($T_{p,max}$) of the iron particle. This approximation is valid because the particle temperature increases almost linearly during the intensive combustion stage where the particle starts to burn shortly before melting [20]. The spectrum-deduced particle peak temperature,[2] measured for the same iron powder under the same environment [20], is adopted to estimate $\langle T_p \rangle$. Because only O_2 and N_2 present in the gas phase, the mass fraction of N_2 at the film layer can be easily calculated once $Y_{O_2,f}$ is determined using Eq. (13). Consequently, the ρ_g and $\mathcal{D}_{O_2,m}$ in the film layer can be readily evaluated. The mixture-averaged $\mathcal{D}_{O_2,m}$ at T_f is evaluated using the open-source software Cantera [40] where the transport properties of O_2 and N_2 included in the kinetic mechanism of Konnov [41] are adopted. The evaluated film layer temperature, O_2 mass diffusivity as well as the molar and mass fractions of O_2 are summaries in Table 1.

Table 1
Estimated temperature and oxygen mass diffusivity at the film layer at different oxygen molar/mass fractions.

$X_{O_2,\infty}$ [−]	$Y_{O_2,\infty}$ [−]	T_f [K]	$\left(\rho_g \mathcal{D}_{O_2,m}\right)_f$ [kg/m/s]
0.10	0.11	1100	5.61×10^{-5}
0.14	0.16	1160	5.82×10^{-5}
0.17	0.20	1200	5.97×10^{-5}
0.21	0.23	1220	6.04×10^{-5}
0.26	0.29	1230	6.07×10^{-5}
0.31	0.34	1240	6.11×10^{-5}
0.36	0.49	1240	6.11×10^{-5}

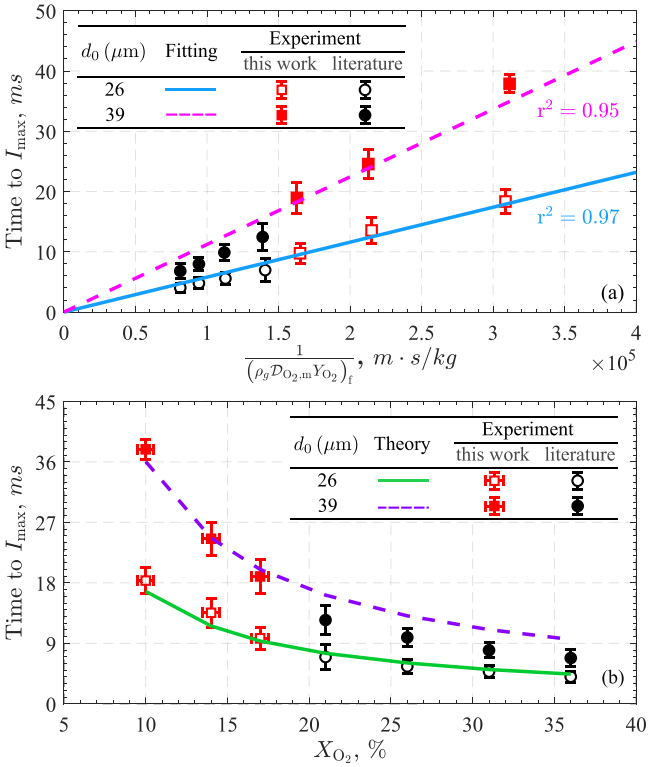

Fig. 11. (a) Time to I_{max} of burning iron particles as a function of the inverse of oxygen mass diffusion flux for two particle diameters of 26 and 39 μm. The fittings are obtained using the linear regression model with zero-intercept (i.e., $y = \kappa x$). (b) Comparison between the theoretically estimated burn time and the experimental time to I_{max} as a function of oxygen molar fractions. The data from literature [19] are for narrow size fractions with mean diameters and standard deviations of 26 ± 3.0 and 39 ± 2.8 μm, respectively. The data obtained in this work are averaged for particle diameters within ±5% deviation of the same mean diameters.

As depicted in Fig. 11(a), the experimental data are well fitted by linear regressions for the smaller particle size. For the larger particle sizes at relatively high O_2 concentrations, the discrepancy is a bit larger likely because of the Stefan flow effect. The nearly linear regression between measured t_{max} and the inverse O_2 diffusion flux suggests that the intensive combustion stage is also limited by external oxygen diffusion under low-oxygen (10–17 vol%) dilution conditions where iron particles mainly burn in the liquid-phase. Moreover, assuming FeO as the combustion product during the intensive burning stage (i.e., S =

[2] When direct measurements are not available, the peak temperature is extrapolated using the fitted correlation between the peak temperature and the oxygen concentration.

3.49 and $\tau = 0.73$), the theoretical burn times of iron particles in the diffusion-limited regime can be calculated using Eqs. (9a) and (9b) and the already estimated values for $\left(\rho_g D_{O_2,m}\right)_f$. Fig. 11(b) shows the comparison between the theoretically calculated burn time with experimental measurements. The newly derived theoretical model well reproduces the current measurement though it has a insignificant over-prediction at elevated O_2 concentrations because the Stefan flow of O_2 towards the particle surface is neglected in the theoretical model. This good agreement not only further identifies the diffusion-limited combustion regime of (> 20 μm) iron particles at a wide range of O_2 levels (at least 10–36 vol%) but also validates the new theoretical model.

6. Conclusions

In the present study, a novel approach of *in situ* particle sizing, based on probing thermal emission during iron melting, is proposed and validated. The approach is also demonstrated to be useful for quantifying the burn time of irregular iron particles as a function of the volume-equivalent diameter. It is then applied to measuring the characteristic timescales of iron particle combustion at diluted oxygen concentrations in the range of 10–17 vol%. Two timescales, namely, total time of light emission (t_{tot}) and time to the maximum light emission intensity (t_{max}), are measured. Both timescales can be described by power-law correlations with $n \in [1.48 \pm 0.11, 1.72 \pm 0.23]$ for t_{max} and $n \in [1.47 \pm 0,12, 1.87 \pm 0.15]$ for t_{tot}, respectively. Furthermore, we derived a generized theoretical model for the burn time of diffusion-limited, heterogeneous particle combustion. The measured t_{max} shows a linear scaling with the external oxygen diffusion flux as suggested by the newly derived theoretical model. This means that the combustion regime of the intensive burning stage is limited by external oxygen diffusion for the currently adopted particle sizes under low-oxygen dilution conditions. Besides, the quantitative agreement between the theory and experiments validates our theoretical model that takes the iron particle expansion during combustion into account.

CRediT authorship contribution statement

D. Ning: Conceptualization, Data curation, Formal analysis, Investigation, Methodology, Software, Validation, Visualization, Writing – original draft, Writing – review & editing. **T. Hazenberg:** Formal analysis, Investigation, Writing – review & editing. **Y. Shoshin:** Formal analysis, Methodology, Supervision, Writing – review & editing. **J.A. van Oijen:** Supervision, Writing – review & editing. **G. Finotello:** Supervision, Writing – review & editing. **L.P.H. de Goey:** Funding acquisition, Project administration, Supervision, Writing – review & editing.

Declaration of competing interest

The authors declare that they have no known competing financial interests or personal relationships that could have appeared to influence the work reported in this paper.

Data availability

Data will be made available on request.

Acknowledgments

This research has received funding from Opzuid (stimulus) Grant agreement no. PROJ-02594. D. Ning acknowledges financial support through Heroes for Heroes Grant no. 1006650 awarded by Eindhoven University of Technology.

Appendix. Derivation of particle density

Given an unburned density (ρ_u), a burned density (ρ_b), and a burned fraction (Y_b), the particle density can be obtained from

$$\rho_p = \frac{\rho_u \rho_b}{\rho_b + Y_b\left(\rho_u - \rho_b\right)}. \tag{A.1}$$

In this equation, it is assumed that the unburned volume (V_u) can be added to the burned volume (V_b) to obtain the particle volume (V_p). The burned fraction is given by

$$Y_b = 1 - \frac{m_u}{m_p}, \tag{A.2}$$

where m_u is the unburned particle mass and m_p is the particle mass. The unburned particle mass is directly related to the mass added to the particle and the stoichiometric ratio S, as

$$m_u = (1+S)\, m_0 - S m_p. \tag{A.3}$$

The unburned mass is substituted into Eq. (A.2) and rewritten

$$Y_b = \frac{(1+S)\, m_p - (1+S)\, m_0}{m_p}, \tag{A.4}$$

which is substituted into Eq. (A.1), giving

$$\rho_p = \frac{\rho_u \rho_b m_p}{\rho_b m_p + \left[(1+S)\, m_p - (1+S)\, m_0\right]\left(\rho_u - \rho_b\right)}. \tag{A.5}$$

Using that

$$m_0 = \frac{1}{6}\rho_u d_0^3 \tag{A.6}$$

and

$$m_p = \frac{1}{6}\rho_p d_p^3, \tag{A.7}$$

Eq. (A.5) is rewritten into

$$\left[\rho_u + S\left(\rho_u - \rho_b\right)\right]\rho_p d_p^3 = \rho_u \rho_b d_p^3 + (1+S)\left(\rho_u - \rho_b\right)\rho_u d_0^3. \tag{A.8}$$

Finally, ρ_p is isolated, which gives

$$\rho_p = \frac{\rho_u \rho_b}{\rho_u + S\left(\rho_u - \rho_b\right)} + \left(\frac{d_0}{d_p}\right)^3 \frac{(1+S)\left(\rho_u - \rho_b\right)\rho_u}{\rho_u + S\left(\rho_u - \rho_b\right)} \tag{A.9}$$

or by introducing $\tau = \rho_b/\rho_u$, it can be written as

$$\rho_p = \rho_1 + \left(\frac{d_0}{d_p}\right)^3 \rho_2 \tag{A.10a}$$

with

$$\rho_1 = \frac{\rho_b}{1 + S(1-\tau)} \tag{A.10b}$$

and

$$\rho_2 = \frac{\left(1 + S^{-1}\right)\left(\rho_u - \rho_b\right)}{1 + S(1-\tau)}. \tag{A.10c}$$

References

[1] Bergthorson JM. Recyclable metal fuels for clean and compact zero-carbon power. Prog Energy Combust Sci 2018;68:169–96.
[2] Julien P, Bergthorson JM. Enabling the metal fuel economy: Green recycling of metal fuels. Sustain Energy Fuels 2017;1(3):615–25.
[3] Debiagi P, Rocha R, Scholtissek A, Janicka J, Hasse C. Iron as a sustainable chemical carrier of renewable energy: Analysis of opportunities and challenges for retrofitting coal-fired power plants. Renew Sustain Energy Rev 2022;165:112579.
[4] Bergthorson J, Goroshin S, Soo M, Julien P, Palecka J, Frost D, et al. Direct combustion of recyclable metal fuels for zero-carbon heat and power. Appl Energy 2015;160:368–82.
[5] Sun J-H, Dobashi R, Hirano T. Combustion behavior of iron particles suspended in air. Combust Sci Technol 1990;150(1–6):99–114.
[6] Sun J-H, Dobashi R, Hirano T. Structure of flames propagating through metal particle clouds and behavior of particles. In: Symposium (international) on combustion. Vol. 27. No. 2. Elsevier; 1998, p. 2405–11.

[7] Sun J-h, Dobashi R, Hirano T. Temperature profile across the combustion zone propagating through an iron particle cloud. J Loss Prev Process Ind 2001;14(6):463–7.
[8] Tang F-D, Goroshin S, Higgins A, Lee J. Flame propagation and quenching in iron dust clouds. Proc Combust Inst 2009;32(2):1905–12.
[9] Tang F-D, Goroshin S, Higgins AJ. Modes of particle combustion in iron dust flames. Proc Combust Inst 2011;33(2):1975–82.
[10] Tóth P, Ögren Y, Sepman A, Gren P, Wiinikka H. Combustion behavior of pulverized sponge iron as a recyclable electrofuel. Powder Technol 2020;373:210–9.
[11] Glassman I, Yetter RA, Glumac NG. Combustion. Academic Press; 2014.
[12] McRae M, Julien P, Salvo S, Goroshin S, Frost DL, Bergthorson JM. Stabilized, flat iron flames on a hot counterflow burner. Proc Combust Inst 2019;37(3):3185–91.
[13] Shoshin YL, Goroshin S, Zolotko A. Flame in a medium with discrete sources. Dokl Phys Chem(Engl Transl);(United States) 1987;291.
[14] Goroshin S, Lee J, Shoshin Y. Effect of the discrete nature of heat sources on flame propagation in particulate suspensions. In: Symposium (international) on combustion. Vol. 27. No. 1. Elsevier; 1998, p. 743–9.
[15] Palečka J, Sniatowsky J, Goroshin S, Higgins AJ, Bergthorson JM. A new kind of flame: Observation of the discrete flame propagation regime in iron particle suspensions in microgravity. Combust Flame 2019;209:180–6.
[16] Ning D, Shoshin Y. Thermal inertia effect of reactive sources on one-dimensional discrete combustion wave propagation. Combust Flame 2023;253:112790.
[17] Poletaev N, Khlebnikova M. Combustion of iron particles suspension in laminar premixed and diffusion flames. Combust Sci Technol 2022;194(7):1356–77.
[18] Wright A, Goroshin S, Higgins A. An attempt to observe the discrete flame propagation regime in aluminum dust clouds. 2015.
[19] Ning D, Shoshin Y, van Oijen JA, Finotello G, de Goey L. Burn time and combustion regime of laser-ignited single iron particle. Combust Flame 2021;230:111424.
[20] Ning D, Shoshin Y, van Stiphout M, van Oijen J, Finotello G, de Goey P. Temperature and phase transitions of laser-ignited single iron particle. Combust Flame 2022;236:111801.
[21] Ning D, Shoshin Y, van Oijen J, Finotello G, de Goey P. Size evolution during laser-ignited single iron particle combustion. Proc Combust Inst 2022.
[22] Ning D, Shoshin Y, van Oijen JA, Finotello G, de Goey LP. Critical temperature for nanoparticle cloud formation during combustion of single micron-sized iron particle. Combust Flame 2022;244:112296.
[23] Li S, Sanned D, Huang J, Berrocal E, Cai W, Aldén M, et al. Stereoscopic high-speed imaging of iron microexplosions and nanoparticle-release. Opt Express 2021;29(21):34465–76.
[24] Li S, Huang J, Weng W, Qian Y, Lu X, Aldén M, et al. Ignition and combustion behavior of single micron-sized iron particle in hot gas flow. Combust Flame 2022;241:112099.
[25] Li T, Heck F, Reinauer F, Böhm B, Dreizler A. Visualizing particle melting and nanoparticle formation during single iron particle oxidation with multi-parameter optical diagnostics. Combust Flame 2022;245:112357.
[26] Panahi A, Chang D, Schiemann M, Fujinawa A, Mi X, Bergthorson JM, et al. Combustion behavior of single iron particles-part I: An experimental study in a drop-tube furnace under high heating rates and high temperatures. Appl Energy Combust Sci 2023;13:100097.
[27] Wright A, Goroshin S, Higgins A. Combustion time and ignition temperature of iron particles in different oxidizing environments. In: International colloquium on the dynamics of explosions and reactive systems. 2015.
[28] Spee T. Toward the design of a mild cyclonic combustor (MC2) for metal fuels (Master's thesis), Eindhoven University of Technology; 2018.
[29] Baigmohammadi M, Prasidha W, Stevens NC, Shoshyn YL, Spee T, de Goey P. Towards utilization of iron powders for heating and power. Appl Energy Combust Sci 2023;13:100116.
[30] Abràmoff MD, Magalhães PJ, Ram SJ. Image processing with ImageJ. Biophotonics Int 2004;11(7):36–42.
[31] Gill RJ, Mohan S, Dreizin EL. Sizing and burn time measurements of micron-sized metal powders. Rev Sci Instrum 2009;80(6):064101.
[32] Feng Y, Xia Z, Huang L, Ma L. Ignition and combustion of a single aluminum particle in hot gas flow. Combust Flame 2018;196:35–44.
[33] Hessels C, Homan T, Deen N, Tang Y. Reduction kinetics of combusted iron powder using hydrogen. Powder Technol 2022;117540.
[34] Ning D, Li T, Mich J, Scholtissek A, Böhm B, Dreizler A. Multi-stage oxidation of iron particles in a flame-generated hot laminar flow. Combust Flame 2023;256:112950.
[35] Finneran J. On the evaluation of transport properties for droplet evaporation problems. Int J Heat Mass Transfer 2021;181:121858.
[36] Frank-Kamenetskii DA. Diffusion and heat exchange in chemical kinetics. Vol. 2171. Princeton University Press; 2015.
[37] van Gool CEAG, Thijs LC, Ramaekers WJS, van Oijen JA, de Goey LPH. Particle Equilibrium Composition model for iron dust combustion. Appl Energy Combust Sci 2023;13:100115. http://dx.doi.org/10.1016/j.jaecs.2023.100115.
[38] Hazenberg T, van Oijen JA. Structures and burning velocities of flames in iron aerosols. Proc Combust Inst 2021;38(3):4383–90. http://dx.doi.org/10.1016/j.proci.2020.07.058.
[39] Thijs L, van Gool CG, Ramaekers W, Kuerten J, van Oijen JA, de Goey L. Improvement of heat-and mass transfer modeling for single iron particles combustion using resolved simulations. Combust Sci Technol 2022;1–17.
[40] Goodwin DG, Moffat HK, Speth RL. Cantera: An object-oriented software toolkit for chemical kinetics, thermodynamics, and transport processes. In: Caltech, Pasadena, CA. Vol. 124. 2009.
[41] Konnov AA. Yet another kinetic mechanism for hydrogen combustion. Combust Flame 2019;203:14–22.